

# A goniometric mask to measure contact angles from digital images of liquid drops



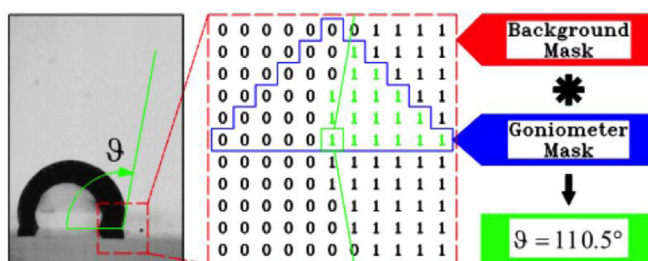
D. Biolè, V. Bertola\*

School of Engineering, University of Liverpool, Brownlow Hill, Liverpool L69 3GH, UK

## HIGHLIGHTS

- We propose a novel image processing method to measure angles in digital images.
- The method requires no edge fitting with analytical curves so is more flexible than other methods.
- The proposed algorithm has low computational cost and has a good robustness to noise.

## GRAPHICAL ABSTRACT



## ARTICLE INFO

### Article history:

Received 12 September 2014  
Received in revised form 30 October 2014  
Accepted 31 October 2014  
Available online 3 December 2014

### Keywords:

Contact angle  
Digital image processing  
Goniometric mask

## ABSTRACT

A computational scheme to measure the inclination angle of apparent edge curves in binary images is proposed. The main concept of the scheme is the emulation of a goniometer tool, which does not require edge fitting with analytic curves for the angle calculation. The algorithm produces an output matrix with same size of the input binary image, where the computed angle values are placed in the same locations of edge pixels. The scheme is tested both on a synthetic binary image displaying an object with irregular contour, and on a stack of images displaying a water droplet impacting on a hydrophobic substrate. The comparison between analytical and calculated angles shows that results depend both on the mask size and, in particular, on the image resolution.

© 2014 Elsevier B.V. All rights reserved.

## 1. Introduction

The contact angle, i.e., the angle between the solid surface and liquid–air interface, measured in the liquid phase, is a fundamental quantity of surface science, and is used to characterise the wettability of solid surfaces, dropwise evaporation or condensation, adhesion between drops and solid surfaces, and several practical applications [1–6]. Contact angle measurement techniques can be sorted into *force tensiometry methods*, which measure the liquid–solid interaction force, and relate it to the contact angle through the Young–Laplace equation [7], and *optical tensiometry*

*methods*, or goniometry methods, where the contact angle is measured directly, generally on a liquid drop in contact with a solid surface [8].

Because force tensiometry methods rely on the Young–Laplace equation, they provide the value of the intrinsic contact angle for a pure fluid at thermodynamic equilibrium with an ideal (i.e., smooth, chemically homogeneous, rigid, insoluble, and non-reactive) solid surface, when the surface and interfacial tensions are known; however, in most practical circumstances the observed (or apparent) contact angle is different from the equilibrium contact angle, and optical methods are preferred. In particular, the contact angle value can be affected by impurities in the fluid [9], line tension [10,11], adsorption of the vapour onto the solid phase [12], electrostatic potential [13], surface roughness [14] or chemical heterogeneity [15], and external forces. Another important case where

\* Corresponding author. Tel.: +44 1517944804.

E-mail address: [Volfango.Bertola@liverpool.ac.uk](mailto:Volfango.Bertola@liverpool.ac.uk) (V. Bertola).

contact angles can be measured only by optical methods is when drops are out of equilibrium. Examples are droplets moving on an inclined surface, or under the action of aerodynamic drag, and drops impinging onto solid surfaces.

In goniometry methods, contact angles are measured from the two-dimensional side view of drops placed on the solid surface, generally by fitting one or more analytical functions to the drop shape, or to a part of it in the neighbourhood of the triple point. For example, in the well-known Axisymmetric Drop Shape Analysis method [16–20] a solution of the Laplace equation is fitted to the drop shape by minimising the error between the theoretical and observed drop boundaries. This technique is also commonly used to measure the interfacial tension (see e.g. [21]). To increase the processing speed, which is desirable to measure dynamic contact angles, circles can be used instead of Laplace curves to fit the drop boundary [22,23], however accuracy is somewhat reduced, especially when the drop size exceeds the capillary length, i.e., when gravity dominates over surface forces, and drops do not take the shape of a spherical cap [24]. These methods require the drop symmetry, which significantly reduces their applicability; moreover, in many cases prior knowledge of the surface tension is also necessary to calculate the approximating Laplace curve.

The local contact angles of non-axisymmetric drops can be calculated for given values of the drop volume and capillary length, when the whole contact line of the drop is known [25]. An obvious limitation of this method is that its accuracy depends on that of the contact line measurement, which may be affected by discretization and/or perspective errors when reconstructed from side views of the drop at different angles [26]. An alternative approach consists in fitting polynomials to find the drop boundary only in a region near the contact line [27–29]. Although the separate analysis of the two edges of the drop allows one to measure contact angles in non-symmetric drops, it prevents the definition of the baseline, which may introduce an error if the baseline is not perfectly horizontal. Furthermore, the method is highly sensitive to the order of the fitting polynomial and the local image resolution. More recently, it was proposed to enhance the precision of polynomial fitting by detecting the position of the drop boundary with sub-pixel resolution [30].

A simple way to fit the edge of asymmetric drops with a single curve is to use piecewise continuous polynomial functions (B-splines) [31,32]. These curves are very flexible, and can fit with high accuracy any drop shape, including strongly non-equilibrium cases such as the first stages of drop impact on a solid surface, provided suitable nodes are selected on the drop edge. However, this makes the method not suitable to analyse large stacks of images, because at present the position of nodes on the drop edge cannot be calculated automatically, but must be specified manually by the algorithm user.

Whilst the above methods can calculate, more or less accurately, the contact angles of drops at equilibrium and of drops in weak non-equilibrium conditions, such as drops moving on an inclined surface, they are not suitable whenever drops are strongly out of equilibrium, for example during the impact on a solid surface [33–35]. In fact, during impact the drop shape undergoes large, rapid, and sometimes non-symmetric deformations, and apparent contact angles cover almost the entire range between  $0^\circ$  and  $180^\circ$ , therefore it is almost impossible to fit with sufficient accuracy the drop shape, or a part of it, in every image of the sequence describing the impact.

This paper describes an image processing method to measure contact angles (or, more in general angles) from digital images based on direct image processing, as if an ideal goniometer was placed directly on the image, without edge fitting. The concept is developed analytically in a Cartesian coordinates system, and then adapted to discretized 2-dimensional domains (matrices). The

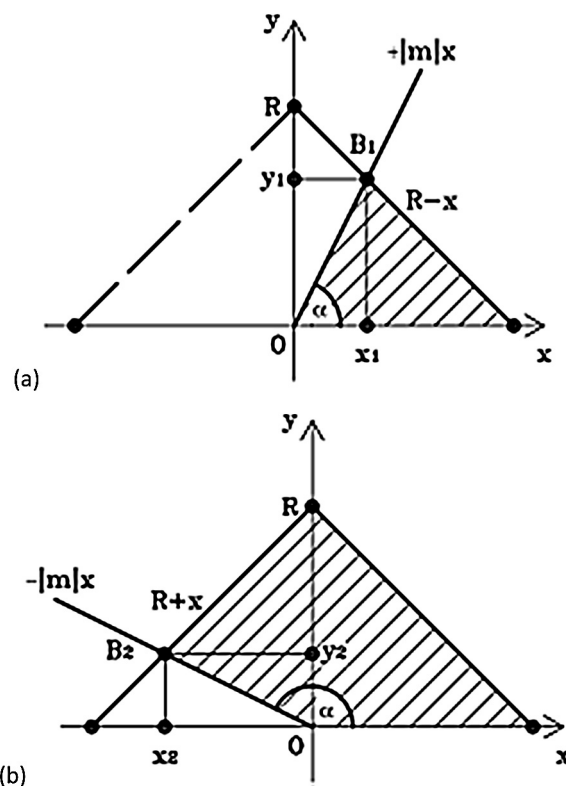


**Fig. 1.** Geometric construction for the derivation of the area-angle formula. (left) Acute angle case; (right) obtuse angle case. The target angle is  $\alpha$ , whilst the computed area  $A$  is filled with inclined straight lines.

method performance is assessed both on a test image defined in terms of analytic functions, and on a stack of images displaying a water droplet impacting on a hydrophobic substrate, captured with a high-speed camera.

## 2. Mathematical formulation

### 2.1. Area-angle relationship

In a Cartesian coordinate system the plane angle  $\alpha$  between the horizontal axis,  $x$ , and the straight line  $y = mx$  is usually expressed as  $\alpha = \tan^{-1}(m)$ . However, the same angle  $\alpha$  can be related to the area of a polygon formed by the horizontal axis,  $x$ , and the straight lines  $y = mx$ ,  $y = R - x$ ,  $y = R + x$ , where  $R$  is a positive constant. The two polygons corresponding to positive and negative values of the angular coefficient,  $m$  (a triangle for  $m > 0$  and a quadrangle for  $m < 0$ ), are displayed in Fig. 1a and b, respectively. Introducing the parameter  $\lambda = \text{sgn}(m)$ , the intercept  $B_\lambda$  of the line  $y = mx$  with either  $y = R - x$  or  $y = R + x$  is defined as:

$$B_\lambda : \begin{cases} y = \lambda |m|x \\ y = R - \lambda x \end{cases} \quad (1)$$

and its coordinates are given by:

$$B_\lambda : \left\{ \frac{\lambda R}{|m| + 1}; \frac{|m|R}{|m| + 1} \right\} \quad (2)$$

Thus, the polygon area can be written in compact form as:

$$A_\lambda = \frac{R^2}{2} \frac{|m| + (1 - \lambda)}{|m| + 1} \quad (3)$$

Using Eq. (3), one can express the tangent of the angle  $\alpha$  as a function of the polygon area and of the sign parameter  $\lambda$ :

$$\tan(\alpha) = \lambda|m| = \lambda \frac{R^2(1-\lambda) - 2A_\lambda}{2A_\lambda - R^2} \quad (4)$$

Finally, since the angle  $\alpha$  varies between 0 and  $\pi$ , while the arctangent function returns values between  $-\pi/2$  and  $\pi/2$ , the relationship between  $\alpha$  and the polygon area is:

$$\alpha = \frac{\pi}{2}(1-\lambda) + \tan^{-1} \left( \lambda \frac{R^2(1-\lambda) - 2A_\lambda}{2A_\lambda - R^2} \right) \quad (5)$$

Thus, the triangle defined by the lines  $y=R \pm x$  and the horizontal axis represents an ideal goniometer, which can measure the angle between a line through the origin of the Cartesian coordinate system and the positive direction of the horizontal axis.

## 2.2. Discrete goniometric mask

To use the ideal goniometer described above with digital images, one must describe it in matrix form, so that the polygon area can be calculated as an operation between matrices. Greyscale images with resolution  $H \times W$  captured by digital cameras are described as two-dimensional matrices, where  $H$  is the number of columns and  $W$  the number of rows; thus, each element of the matrix  $I_5$ , defined by the row number  $i$  and the column number  $j$ , corresponds to a unique pixel in the image, and its value represents the pixel intensity (e.g., in 8-bit images  $I_5(i,j)=0$  corresponds to black and  $I_5(i,j)=255$  corresponds to white). For practical purposes, image matrices can be normalised so that all pixel values are between 0 and 1.

Digital images from high-speed cameras are often dark, with low contrast and resolution, as shown in the example displayed in Fig. 2a, therefore pre-processing is necessary to enhance the image quality. Although in the open literature there is a wealth of filters to increase the image resolution by interpolation and to adjust brightness and/or contrast [36,37], the optimal choice of their parameters still requires the visual observation of images, therefore is not objective and may vary for large stacks of images. Thus, when a reference image (i.e., an image without the liquid drop in the same illumination conditions) is available, background subtraction is preferable [38]. The fluid–fluid interface, or the drop contour, can be obtained with high accuracy using the Canny algorithm [39]; an example of pre-processed image is displayed in Fig. 2b, where the drop contour is highlighted by a solid black line. Once the drop contour has been defined, it is trivial to convert the original image into a black-and-white binary image (Fig. 2c).

The method described in Section 2.1 above can be used to measure the angle between the tangent line to any point of a contour line in a generic binary image and the horizontal axis. In fact, Eq. (5) demonstrates that such angle is related to a certain area, determined from the intersection of the object defined by the contour line of interest, and a suitable reference triangle; the area is then measured by counting the number of pixels in the region where the object and the triangle overlap. To do so, one can superimpose to the original image a smaller binary image representing a triangle (hence the name *goniometric mask*) in such a way that the midpoint of the triangle base corresponds to the point of interest on the contour line, as shown in Fig. 3a. To ensure the triangle symmetry, the size of the goniometric mask must be an odd integer. One can easily verify that, if the contour line divides the triangle in two parts only (i.e., the triangle is sufficiently small), the shaded areas in Fig. 1a and b correspond, on the digital image, to those areas where the pixels value is 1 both on the image and on the goniometric mask; then, the numeric value of the area is simply the sum of the matrix elements corresponding to these pixels. In particular, if the mask

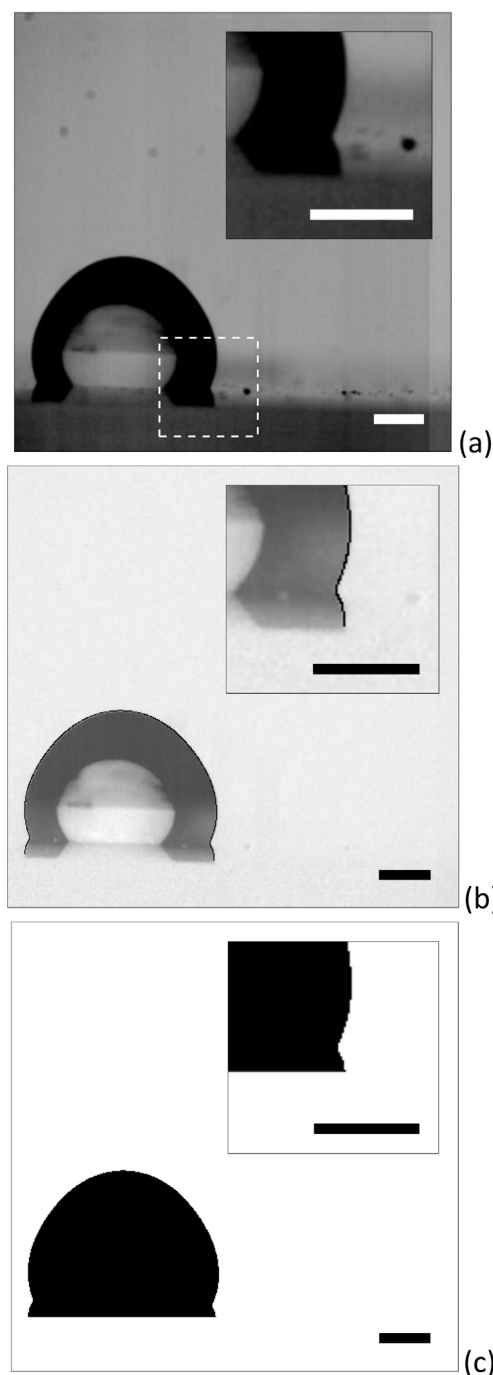


**Fig. 2.** Impact of a water drop on a fluoropolymer coated glass slide,  $t=50$  ms after impact; length bars 1 mm. (a) Original image – (b) image purged by the background; the black solid line is the interface, i.e., the edge of the drop – (c) binary image.

is placed on the point where the drop contour meets the substrate, the measured area corresponds to the contact angle.

In the case of binary images, the count of pixels falling within this area can be obtained with a simple 2-dimensional convolution operation; in fact, the discrete convolution operator between two matrices  $A$  and  $B$  yields a matrix whose elements are the sums of the products of the elements of  $A$  and  $B$ . Since convolution takes the rows and columns of the second matrix in reverse order, the goniometric mask must be flipped both vertically and horizontally, as shown in Fig. 3b. Thus, the general matrix form of the goniometric mask is given by Eq. (6), where the mask size, i.e., the number of

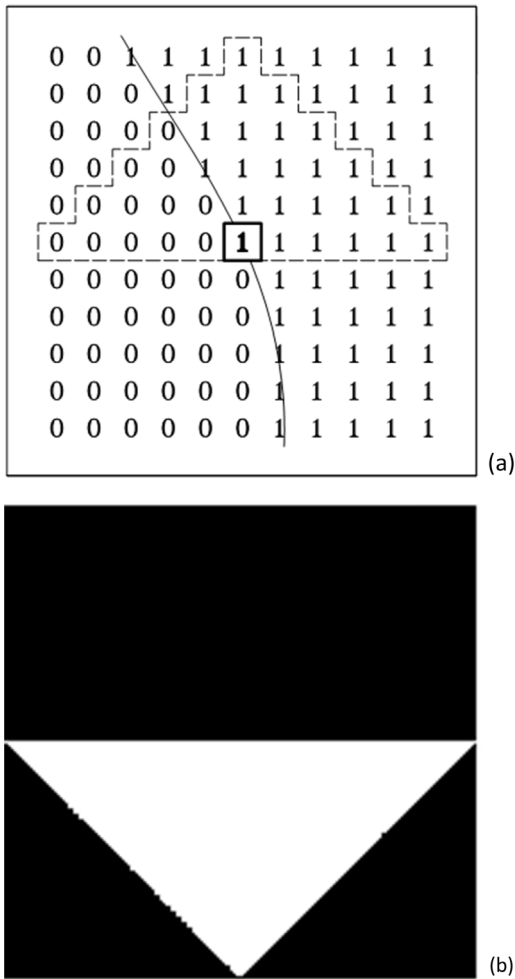


**Fig. 3.** Sampling window of the binary image matrix (a). The continuous line indicates the ideal contour line, the dashed line encloses the elements considered for the area-angle calculation, and the boxed element corresponds to the pixel where the tangent inclination is measured. (b) Image generated by the mask matrix.

rows or column of the matrix, or the number of pixels of a side of the corresponding image, is  $2n + 1$ , where  $n$  is an integer number.

$$M = \begin{bmatrix} 0 & 0 & 0 & \dots & 0 & 0 & 0 \\ \vdots & \vdots & \vdots & \dots & \vdots & \vdots & \vdots \\ 0 & 0 & 0 & \dots & 0 & 0 & 0 \\ 1 & 1 & 1 & \dots & 1 & 1 & 1 \\ 0 & 1 & \dots & 1 & \dots & 1 & 0 \\ \vdots & 0 & \ddots & 1 & \ddots & 0 & \vdots \\ 0 & \dots & 0 & 1 & 0 & \dots & 0 \end{bmatrix} \quad (6)$$

The optimal choice of the mask size is a result of a trade-off between the need to follow the contour line curvature, which requires a small mask, and accuracy in the area measurement, which requires a bigger mask.

### 2.3. Image masking

When the mask matrix  $M$  is convolved with the complementary matrix of an arbitrary binary image  $I_S$  (Eq. (7)), each element

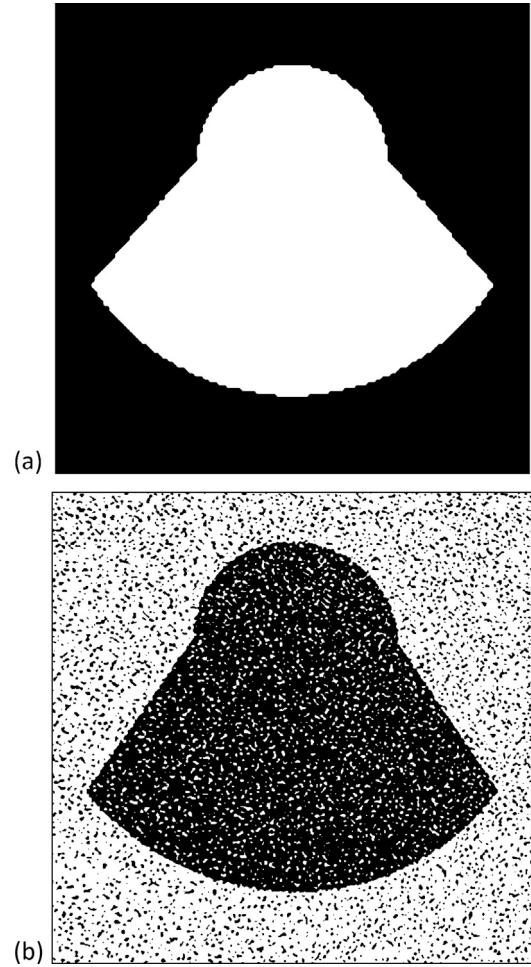


**Fig. 4.** (a) Synthetic test image generated by the analytical functions in Table 1. (b) The same image perturbed by a Gaussian noise (SNR = 0.7).

of the resulting matrix  $A$  represents the count of a portion of the background pixels of  $I_S$  falling into the triangular shape of the mask:

$$A(r, c) = \sum_{i=0}^{2n} \sum_{j=0}^{2n} I_S(r-i, c-j) M(i, j) \quad (7)$$

where  $r$  and  $c$  denote the current element row and column, respectively; if  $M$  is defined as in Section 2.2, the background portion has size  $(2n + 1) \times (2n + 1)$ , whilst  $A$  has size  $(H + 2n) \times (W + 2n)$ .

It must be remarked that the angle-area relationship derived in Section 2.1 above for a triangular shape could be obtained, with a similar procedure, for other shapes as well (e.g., a half-circle). However, the triangular shape offers a number of advantages when discretised, including a weaker dependence of results on the mask size and a significantly lower computational cost of the convolution operation. This happens because among all shapes that can be constructed inside a square matrix, the triangle is the convex shape enclosing the smallest number of elements, hence there are less non-zero elements involved in operations.

## 3. Validation

### 3.1. Validation of synthetic images

The algorithm was initially tested on the synthetic image displayed in Fig. 4a, defined by the piecewise contour line given in Table 1, and with a resolution  $H = 400 \times 400$  pixels, using a



**Table 1**  
Analytical definition of the synthetic test image.

Function	Range	1st derivative
$y_1 = y_C - \sqrt{r_1^2 - (x - x_C)^2}$	$x_C - r_1 \leq x \leq x_C + r_1$	$y'_1 = -\frac{x - x_C}{y_1 - y_C}$
$y_2 = y_C + (x - x_C - r_1) \frac{\sqrt{1 - k^2}}{k - r_1/r_3}$	$x_C + r_1 < x < x_C + kr_3$	$y'_2 = \frac{\sqrt{1 - k^2}}{k - r_1/r_3}$
$y_3 = y_C + \sqrt{r_3^2 - (x - x_C)^2}$	$x_C - kr_3 < x < x_C + kr_3$	$y'_3 = -\frac{x - x_C}{y_3 - y_C}$
$y_2 = y_C - (x - x_C + r_1) \frac{\sqrt{1 - k^2}}{k - r_1/r_3}$	$x_C - kr_3 < x < x_C - r_1$	$y'_2 = -\frac{\sqrt{1 - k^2}}{k - r_1/r_3}$

goniometric mask of size  $z=21$  pixels. Fig. 5a shows the comparison between measured angles, corresponding to the slope of the tangent line in each point of the image contour, and their analytical values, calculated from the contour line equations in Table 1. The difference between the two values, is always very small and uniform everywhere along the test contour line, except for the small number of points where cusps falls within the triangle of the goniometric mask. In fact, in this case the mask contains two lines with different slope, and the resulting angle is the difference between the inclinations of these lines with respect to the horizontal axis. When the mask is centred exactly on the cusp, there is no error. One can also observe that measurements in Fig. 5a tend to align on two parallel lines, one of which is the 45° line indicating coincidence between the analytical and measured values, and one slightly displaced; in particular, pairs of symmetric points on the test image contour correspond to one measurement on each of these lines. This happens because, depending on the relative position of the mask and the contour, measurements are

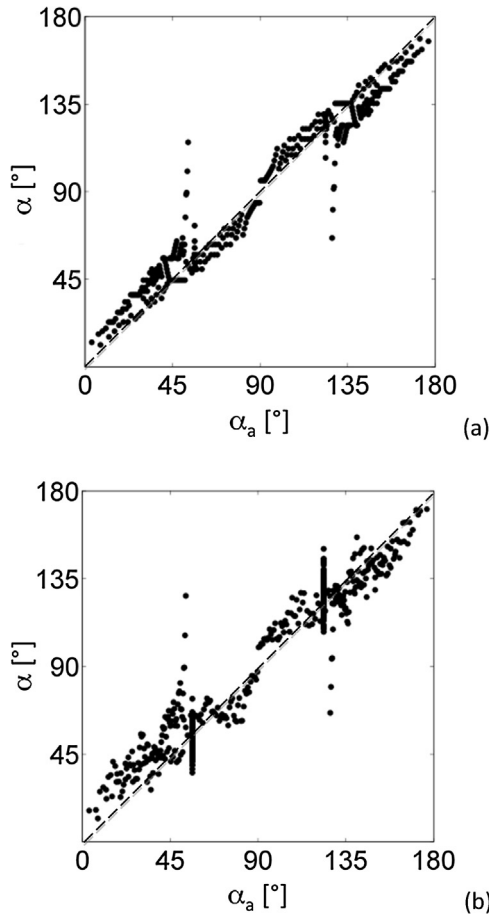


**Fig. 5.** Comparison between the measured angle and the analytical value. (b) Original image (Fig. 4a), (b) perturbed image (Fig. 4b).

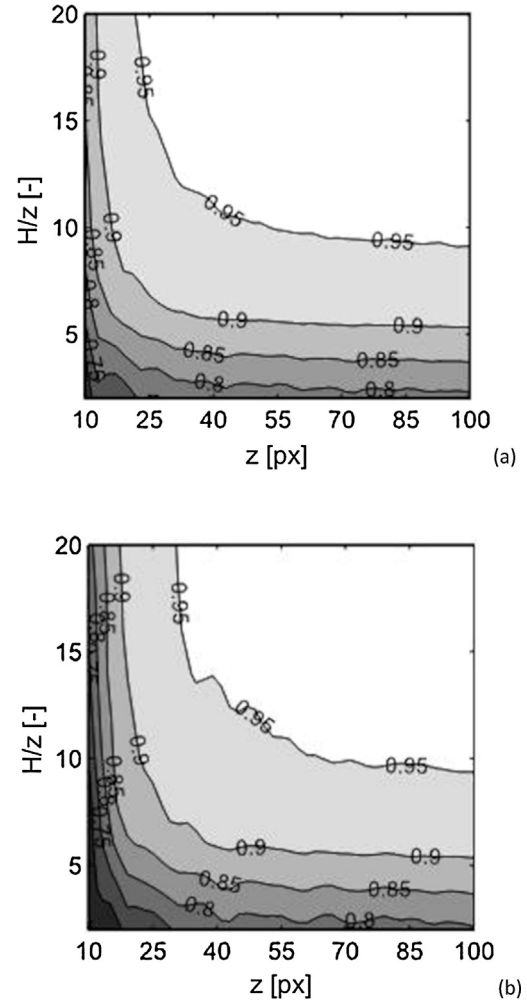


**Fig. 6.** Contour maps of the determination coefficient ( $R^2$ ) relative to the difference between analytical and measured angles, as a function of the mask size and the image/mask size ratio.

slightly more accurate when the associated area is bigger (e.g., compare Figs. 1b and 2a) because of pixel discretisation; such error source can be easily dealt with, for example, by flipping the image.

The mask size,  $z$ , strongly affects the angle measurement because a discrete mask can resolve a maximum number of discrete angle values equal to the number of pixels in the triangle,  $(z+1)^2/4$ . Thus, the minimum value (in radians) that can be measured, corresponding to one pixel, is  $4\pi/(z+1)^2$ ; for example, to measure an angle of  $1^\circ$ , the mask size should be  $z = 2\sqrt{180} - 1 \approx 25$ . In addition, the relative size of the mask to that of the image (the ratio  $z/H$ ) is also important, as mentioned in Section 2.2 above. Fig. 6a displays the contour map of the coefficient of determination ( $R$ -squared) for measured angles with respect to analytical angles, obtained from 2116 points with different values of  $z$  and  $H/z$ . As expected, the algorithm performance is a trade-off between the input parameters; on one hand, increasing the mask size pays back in terms of accuracy but, on the other hand, if the image size to mask size ratio is too small angles are not measurable. Overall, very good accuracies can be achieved with masks as small as  $20 \times 20$  pixels, provided the image is at least 6/7 times bigger.

To test the angle measurement algorithm robustness, a Gaussian noise with standard deviation of 0.36, was also added to the synthetic test image, as shown in Fig. 4b; this results into a signal to noise ratio (SNR) of 0.7. When noise is added to the image, the average error grows (Fig. 5b), however measured angles are

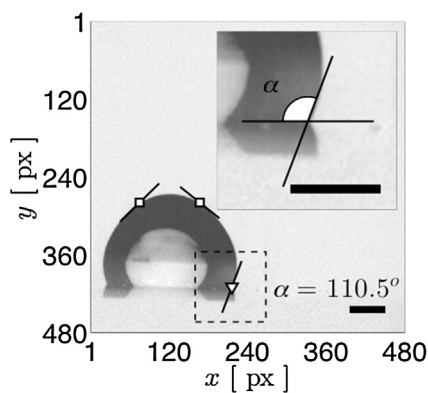


**Fig. 7.** Example of contact angle and tangent line measurements on the image of a sessile drop.

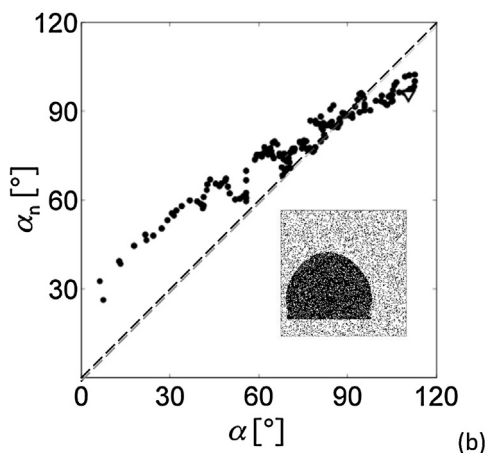
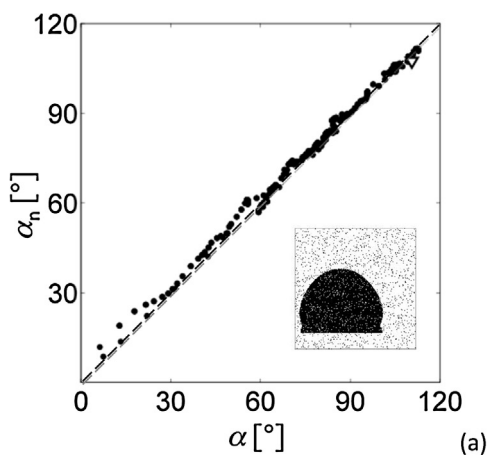


**Fig. 8.** Comparison between angles measured on the binary image obtained from Fig. 7 ( $\alpha$ ) and on the perturbed images displayed in the insets ( $\alpha_n$ ). (a) SNR = 31.33 dB; (b) SNR = 16.51 dB (b).

uniformly scattered around the analytical value, so that averaging over a set of neighbouring points of the contour line would significantly improve the accuracy of results. This is confirmed by the coefficient of determination map displayed in Fig. 6b, which shows how in general masks of bigger size are required when the algorithm is applied to noisy images, to achieve the same coefficient of determination of measurements on images without noise; in fact, increasing the mask size is equivalent to average the angle calculation over a longer chord of the test image contour.

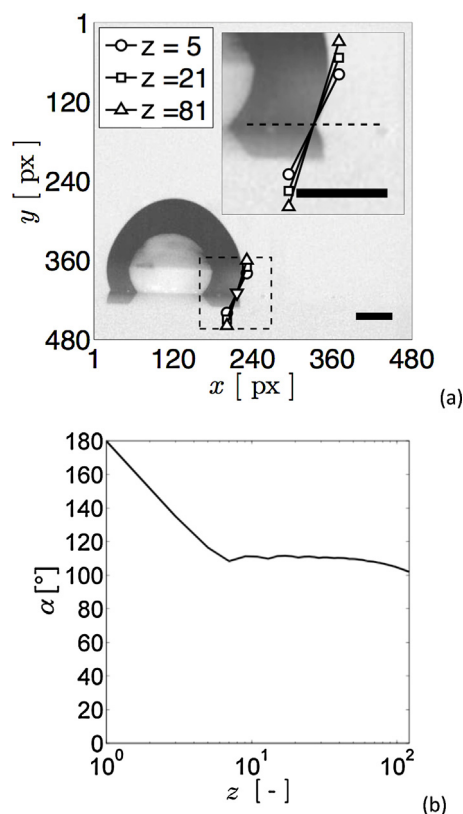


**Fig. 9.** Effect of the mask size on the angle measurement. (a) Graphical construction of three tangent lines in the contact point, corresponding to different mask sizes. (b) Measured angle as a function of the mask size.

### 3.2. Validation on real images

To assess the algorithm performance on real drop images, it was applied used to measure both the inclination of the tangent to the contour line and the contact angle of the drop displayed in Fig. 2a, extracted from a stack of images captured at 5000 fps describing the impact of a water droplet ( $D \sim 3$  mm) on a hydrophobic surface (a glass slide dip coated with Cytonix Fluoropel PFC1302A fluoropolymer solution,  $\theta_{eq} \sim 110^\circ \pm 3^\circ$ ) with an impact Weber number ( $We = \rho u^2 D / \sigma$ , where  $\rho$  is the fluid density,  $u$  is the drop impact velocity, and  $\sigma$  is the surface tension) equal to 14, and corresponding to a time of 50 ms after impact. The image resolution was  $480 \times 480$  pixels (corresponding to about 54 pixels/mm), while the mask size was  $z = 21$  pixels.

Fig. 7 displays the inclination of the tangent line in three points on the contour of the original image after background subtraction, including the contact point with the substrate, where the apparent contact angle is calculated. In particular, the value obtained here ( $110.5^\circ$ ) is in perfect agreement with the range indicated by the fluorinated coating supplier.

The algorithm was then used to calculate the slope of the tangent line in every point of the drop contour. These values were compared with the corresponding values obtained by adding a random noise to the image, with signal to noise ratios of 31.33 dB (Fig. 8a) and 16.51 dB (Fig. 8b), respectively. For a relatively large SNR (i.e., weak noise level), which is the case, for example, of flickering images extracted from high-speed movies, the algorithm is not affected by noise and still provides identical results to those obtained from images without noise. However, when the SNR is significant measurements are accurate only when  $\alpha \approx 90^\circ$ , and one can observe significant errors for the smaller ( $\alpha < 60^\circ$ ) and the larger ( $\alpha > 100^\circ$ ) angle values. This can be somewhat improved by increasing the

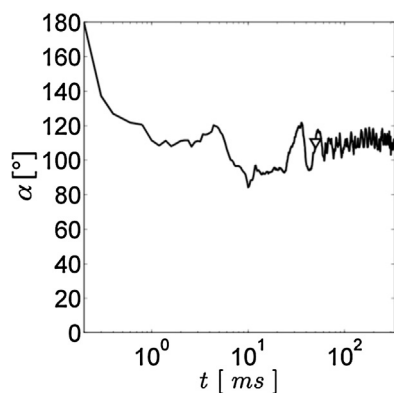


Fig. 10. Apparent dynamic contact angle measured with a mask size  $z=21$ ; the triangle corresponds to the frame discussed in Figs. 7–9.

mask size, which is equivalent to averaging the angle measurement over a longer chord of the contour line.

The effect of the mask/image size ratio is shown in Fig. 9. In particular, in Fig. 9a the contact angle is compared for three mask sizes very different from one another ( $z=5$ , 21 and 81); as one can see from this figure, all of the three tangent lines reasonably fit the drop shape, including the one obtained from the smallest mask ( $z=5$ ). This value, corresponding to a digital triangle built with three rows of 5, 3 and 1 pixels, respectively, is the minimum mask size that yields significant measurements (with  $z=3$ , the triangle consists of two rows of 3 and 1 pixels only). More in detail the measured value, displayed as a function of the mask size in Fig. 9b, reaches a constant value for  $z>5$ , but when the mask size becomes comparable with the image size (in this case,  $z>50$ ) it starts decreasing again. Thus, one can conclude the optimum mask size can be located at the beginning of the plateau of this curve, i.e., the minimum size that yields angle measurements independent of the mask size. The actual value of the mask size can be further tuned depending on other constraints; for example, measuring very small angles ( $<1^\circ$ ) require larger masks ( $z>25$ ), whereas smaller masks ( $5<z<20$ ) can be used for images with poor resolution.

Finally, Fig. 10 displays the dynamic contact angle of the impacting drop as a function of time, obtained by processing the entire stack of images. These results are in very good agreement with other literature data on dynamic contact angle measurements [33,34,40], although a direct comparison is obviously not possible because of the different experimental conditions.

#### 4. Conclusions

A novel image processing method to measure the apparent contact angle from side views of drops in contact with a solid surface was developed based on the concept of goniometric mask, i.e., an auxiliary matrix that is convolved with the image matrix. Unlike most of the existing methods, the proposed algorithm relies entirely on digital image processing, and does not require drop edge fitting with analytical curves.

The advantages of this method are: a high flexibility, which allows one to measure not only the contact angle, but also the tangent slope at any point of a given interface displayed in a digital image; the ability to measure accurately very small angles and/or to deal with large curvatures of the interface, for example those observed during drop impact on solid surfaces and in dynamic wetting of superspreader surfactant solutions; a low computational cost, which makes it suitable to process large stacks of images, such as those generated by state-of-the-art high-speed cameras, in a relatively short time.

#### Acknowledgement

This work was supported by the University of Liverpool – A\*STAR (Singapore) partnership.

#### References

- [1] P.-G. de Gennes, Wetting: statics and dynamics, *Rev. Mod. Phys.* 57 (1985) 827–863.
- [2] R. Förch, H. Schönherr, A. Tobias, A. Jenkins, *Surface Design: Applications in Bioscience and Nanotechnology*, Wiley-VCH, 2009, ISBN 3-527-40789-8.
- [3] G. McHale, S.M. Rowan, M.I. Newton, M.K. Banerjee, Evaporation and the wetting of a low energy surface, *J. Phys. Chem. B* 102 (1998) 1964–1967.
- [4] G. Kugel, T. Klettke, J.A. Goldberg, J. Benichmol, R.D. Perry, S. Sharma, Investigation of a new approach to measuring contact angles for hydrophilic impression materials, *J. Prosthodont.* 16 (2007) 84–92.
- [5] D. Daffonchio, J. Thaveesri, W. Verstraete, Contact angle measurement and cell hydrophobicity of granular sludge from upflow anaerobic sludge bed reactors, *J. Appl. Environ. Microbiol.* 61 (1995) 3676–3680.
- [6] F. Salaun, E. Devaux, S. Bourbigot, P. Rumeau, Application of contact angle measurement to the manufacture of textiles containing microcapsules, *Text. Res. J.* 79 (2009) 1202–1212.
- [7] J.K. Spelt, A.W. Neumann, *Applied Surface Thermodynamics*, Dekker, New York, 1996, pp. 379–412.
- [8] Y.P. Gu, Contact angle measurement techniques for determination of wettability, in: P. Somasundaran, A. Hubbard (Eds.), *Encyclopedia of Surface and Colloid Science*, Taylor & Francis, 2006.
- [9] H.N. Oğuz, S.S. Sadhal, Effects of soluble and insoluble surfactants on the motion of drops, *J. Fluid Mech.* 194 (1988) 563–579.
- [10] A. Marmur, Line tension and the intrinsic contact angle in solid–liquid–fluid systems, *J. Colloid Interface Sci.* 186 (1997) 462–466.
- [11] A.I. Rusanov, Classification of line tension, *Colloids Surf. A* 156 (1999) 315–322.
- [12] S. Baxter, Wetting and contact-angle hysteresis, *Nature* 165 (1950) 198.
- [13] K.H. Kang, How electrostatic fields change contact angle in electrowetting, *Langmuir* 18 (2002) 10318–10322.
- [14] R.N. Wenzel, Surface roughness and contact angle, *J. Phys. Colloid Chem.* 53 (1949) 1466–1467.
- [15] A.B.D. Cassie, Contact angles, *Discuss. Faraday Soc.* 3 (1948) 11–16.
- [16] Y. Rotenberg, L. Boruvka, A.W. Neumann, Determination of surface tension and contact angle from the shapes of axisymmetric fluid interfaces, *J. Colloid Interface Sci.* 93 (1983) 169–183.
- [17] O.I. del Rio, A.W. Neumann, Axisymmetric drop shape analysis: computational methods for the measurement of interfacial properties from the shape and dimensions of pendant and sessile drops, *J. Colloid Interface Sci.* 196 (1997) 136–147.
- [18] A. Kalantarian, R. David, A.W. Neumann, Methodology for high accuracy contact angle measurement, *Langmuir* 25 (2009) 14146–14154.
- [19] A. Bateni, S.S. Susnar, A. Amirfazli, A.W. Neumann, Development of a new methodology to study drop shape and surface tension in electric fields, *Langmuir* 20 (2004) 7589–7597.
- [20] M. Hoorfar, A.W. Neumann, Recent progress in axisymmetric drop shape analysis (ADSA), *Adv. Colloid Interface Sci.* 121 (2006) 25–49.
- [21] E. Atefi, J. Adin Mann, H. Tavana, Ultralow interfacial tensions of aqueous two-phase systems measured using drop shape, *Langmuir* 30 (2014) 9691–9699.
- [22] L. Li, W. Kang, D. Ye, A contact angle measurement method for the droplets in EWOD-based chips, in: *Proc. 2nd IEEE, Conf. Nano/Micro Eng. Molec. Sys.*, Bangkok, Thailand, 16th–19th January, 2007.
- [23] J. Goclawski, W. Urbaniak-Domagala, The method of solid–liquid contact angle measurement using the images of sessile drops with shadows on substratum, in: *Proc. Memstech Lviv-Polyana, Ukraine*, 23rd–26th May, 2007, pp. 135–140.
- [24] M. Bortolotti, M. Brugnara, C.D. Volpe, S. Siboni, Numerical models for the evaluation of the contact angle from axisymmetric drop profiles: a statistical comparison, *J. Colloid Interface Sci.* 336 (2009) 285–297.
- [25] S. Iliiev, N. Pesheva, Nonaxisymmetric drop shape analysis and its application for determination of the local contact angles, *J. Colloid Interface Sci.* 301 (2006) 677–684.
- [26] S.F. Chini, V. Bertola, A. Amirfazli, A methodology to determine the adhesion forces of arbitrarily shaped drops with convex contact lines, *Colloids Surf. A: Physicochem. Eng. Asp.* 436 (2013) 425–433.
- [27] A. Bateni, S.S. Susnar, A. Amirfazli, A.W. Neumann, Effect of electric fields on contact angle and surface tension of drops, *Colloids Surf. A* 219 (2003) 215–231.
- [28] S. Schuetter, T. Shedd, K. Dostator, G. Nellis, C. Van Peski, A. Grenville, S.H. Lin, D.C. Owe-Yang, Measurements of the dynamic contact angle for conditions relevant to immersion lithography, *J. Microlithogr. Microfabr. Microsyst.* 5 (2006) 023002.
- [29] E. Atefi, J. Adin Mann, H. Tavana, A robust polynomial fitting approach for contact angle measurements, *Langmuir* 29 (2013) 5677–5688.
- [30] S.F. Chini, A. Amirfazli, A method for measuring contact angle of asymmetric and symmetric drops, *Colloids Surf. A: Physicochem. Eng. Asp.* 388 (2011) 29–37.
- [31] A.F. Stalder, G. Kulik, D. Sage, L. Barbieri, P. Hoffmann, A snake-based approach to accurate determination of both contact points and contact angles, *Colloids Surf. A* 286 (2006) 92–103.

- [32] C. Xu, J.L. Prince, Snakes, shapes, and gradient vector flow, *IEEE Trans. Image Process.* 7 (March) (1998) 359–369.
- [33] I.S. Bayer, C.M. Megaridis, Contact angle dynamics in droplets impacting on flat surfaces with different wetting characteristics, *J. Fluid Mech.* 558 (2006) 415–449.
- [34] V. Bertola, The effect of polymer additives on the apparent dynamic contact angle of impacting drops, *Colloids Surf. A: Physicochem. Eng. Asp.* 363 (2010) 135–140.
- [35] V. Bertola, Dynamic wetting of dilute polymer solutions: the case of impacting droplets, *Adv. Colloids Interfaces* 193–194 (2013) 1–11.
- [36] W. Burger, M.J. Burge, *Digital Image Processing*, 1st ed., Springer, 2008.
- [37] M. Nixon, A.S. Aguado, *Feature Extraction & Image Processing for Computer Vision*, Elsevier Science, 2012.
- [38] M. Piccardi, Background subtraction techniques: a review, *IEEE Int. Conf. Syst. Man Cybern.* 4 (2004) 3099–3104.
- [39] J. Canny, A computational approach to edge detection, *IEEE Trans. Pattern Anal. Mach. Intell.* 8 (1986) 679–698.
- [40] H. Wang, P.J. Mucha, G. Turk, Water drops on surfaces, *ACM Trans. Graph.* 24 (2005) 921.